Large-Eddy Simulation of a Wing Tip Vortex on Overset Grids

Ali Uzun[*] and M. Yousuff Hussaini[†]
Florida State University, Tallahassee, Florida 32306-4120
and
Craig L. Streett[‡]
NASA Langley Research Center, Hampton, Virginia 23681

A multiblock large-eddy simulation (LES) code with overset grid capability is reported on that has been developed primarily to study the tip vortex noise problem arising on rotating wind-turbine blades. The LES code can also be used to simulate the tip vortices around nonrotating wing geometries typically found in aeronautical applications. It employs state-of-the-art compact finite differencing, implicit spatial filtering, and nonreflecting boundary conditions on free boundaries, as well as characteristic-type boundary conditions on solid walls. High-order-accurate interpolation is used for the transfer of information among the individual component grids that make up the overset grid topology. The multiblock nature and the overset grid capability of the code allow high-order accurate numerical solutions in complex domains. Results for the tip vortex around a nonrotating wing with a rounded tip are presented to demonstrate the capability of the code. Comparisons of the numerical results with experimental data are also carried out.

Nomenclature

b	=	wing span
Cp_{static}	=	static pressure coefficient
Cp_{total}	=	total pressure coefficient
c	=	wing chord length
D	=	spatial derivative
e_t	=	total energy, $\rho(u^2 + v^2 + w^2)/2 + p/(\gamma - 1)$
$\boldsymbol{F}, \boldsymbol{G}, \boldsymbol{H}$	=	inviscid flux vectors in Navier–Stokes equations
$\boldsymbol{F}_v, \boldsymbol{G}_v, \boldsymbol{H}_v$	=	viscous flux vectors in Navier–Stokes equations
f	=	arbitrary variable
i, j, k	=	grid point indices
$\boldsymbol{i}, \boldsymbol{j}, \boldsymbol{k}$	=	unit vectors in Cartesian coordinates
J	=	metric Jacobian
K	=	turbulent kinetic energy
N	=	number of grid points along given spatial direction
p	=	static pressure
p_{total}	=	total pressure, $p + \rho(u^2 + v^2 + w^2)/2$
Q	=	vector of conservative flow variables
$\boldsymbol{Q}$	=	Q/J
Re_c	=	wing chord Reynolds number, $\rho_\infty u_\infty c/\mu_\infty$
t	=	time
u, v, w	=	Cartesian velocity components in x, y, and z directions
u_τ	=	friction velocity, $\sqrt{(\tau_{\text{wall}}/\rho)}$
x, y, z	=	Cartesian coordinates in streamwise, vertical, and spanwise directions
α_f	=	filtering parameter
γ	=	ratio of specific heats of air, 1.4
Δt	=	time increment
ΔW	=	wall normal grid spacing
$\Delta \xi$	=	uniform grid spacing along ξ direction in computational domain
ϵ_I	=	artificial dissipation parameter in implicit time stepping
μ	=	molecular viscosity
ν	=	kinematic viscosity, μ/ρ
ξ, η, ζ	=	generalized curvilinear coordinates
ρ	=	fluid density
σ_{ijk}	=	spectral radius of inviscid flux Jacobian at grid point, i, j, k
τ_{wall}	=	wall shear stress
$\langle \rangle$	=	time averaging operator

Subscripts

i	=	value at grid point i
∞	=	freestream value

Superscripts

B	=	backward operator in prefactored optimized compact scheme
F	=	forward operator in prefactored optimized compact scheme
n	=	time level
p	=	subiteration level
$+$	=	value given in wall units
$'$	=	perturbation from mean value
$-$	=	spatially filtered quantity
$\sim$	=	Favre-filtered quantity

*Postdoctoral Research Associate, School of Computational Science. Senior Member AIAA.
†Sir James Lighthill Professor of Mathematics and Computational Science and Engineering, School of Computational Science.
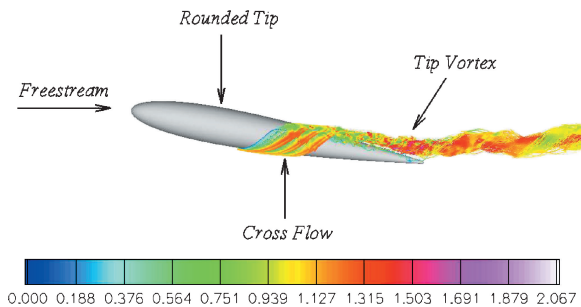‡Senior Research Scientist, Computational Aerosciences Branch.

I. Introduction

TIP vortex noise is a problem that is commonly encountered with the airflow around rotating blades (such as wind-turbine or helicopter blades), as well as nonrotating wing geometries and flap side edges of high-lift systems found in aeronautical applications. Because of the pressure differences between the suction and pressure sides of the blade tip (or the wing tip), a crossflow over the side edge of the tip occurs and gives rise to the formation of a tip vortex as shown in Fig. 1. The interaction of the tip vortex with the side edge and the trailing edge of the tip results in the so-called tip noise. Control and minimization of tip vortex noise are important for the future design of quieter wind-turbine blade tips and other applications such as aircraft high-lift systems that could benefit from such technological advances. Yet the physical

Fig. 1   Streamlines showing formation of tip vortex around rounded tip geometry; freestream flow approaches tip geometry at Mach number of 0.15 and angle of attack of 10 deg, where colors denote magnitude of instantaneous axial velocity normalized by freestream velocity.

mechanisms of tip noise generation are still not well understood, and there is need for its further investigation. Even without its noise aspect, the tip vortex is still important because it plays a significant role in other problems such as the landing separation distance for aircraft and the vibration caused by blade–vortex interaction on helicopter blades. A better understanding of the physics of the tip vortex is, therefore, crucial for the mitigation of its undesirable effects (such as noise, vibration, and landing distance separation) in various applications.

The significance of the tip vortex has motivated numerous experimental studies. An in-depth review of various tip vortex experiments is provided by Chow et al.[1] or Chow.[2] Such experiments have usually concentrated on the mean flow of the vortex and, in some cases, turbulence measurements. An experimental work aimed toward the study of tip vortex noise arising on aircraft high-lift systems was conducted by Radeztsky et al.[3] and focused on detailed measurements of a flap side edge flowfield. Although experiments are essential and provide useful data, they can supply only a limited amount of information. Properly validated computational techniques, on the other hand, have the potential to provide much more detail about the problem of interest. The recent improvements in the processing speed of computers have indeed made numerical techniques quite useful and popular in the study of various aerodynamics and aeroacoustics problems of interest. For example, regarding the tip vortex problem, the studies by Dacles-Mariani et al.[4,5] as well as that by Kim and Rhee[6] have used Reynolds-averaged Navier–Stokes (RANS) type simulations to study the mean flowfield of the vortex around the rounded tip of a NACA0012 wing with good success. Takallu and Laflin[7] as well as Khorrami et al.[8] have also used RANS calculations to study the tip vortex formation around flap side edges in high-lift systems. However, if the goal is to predict noise, then the use of RANS for noise prediction becomes questionable because RANS methods heavily rely on turbulence models to model all of the relevant turbulence scales. Moreover, such methods try to predict the noise using the mean flow properties provided by a RANS solver. Because noise generation is a multiscale problem that involves a wide range of length and timescales, it appears that the success of RANS-based noise prediction methods will remain limited to specific cases for which semiempirical noise models exist. One specific case where RANS-based methods have been particularly successful is axisymmetric subsonic jet noise. Presently, there is no semiempirical noise model available for tip vortex noise and, to our best knowledge, there has not been any attempt to compute the tip vortex noise using RANS either.

Large-eddy simulation (LES) techniques, although still computationally expensive, are becoming increasingly popular in computational aeroacoustics (CAA) research because such methods can directly resolve a portion of the energy containing turbulent eddies, which are believed to be the primary noise generating sources. LES depends much less on turbulence models because a portion of the energy containing range of eddies are directly resolved, and only the unresolved or subgrid-scales need to be modeled. Thus far, LES has been successfully applied to various aeroacoustics problems of in-

terest such as jet noise, airfoil trailing-edge noise, and cavity noise, to mention a few applications. Such studies show the attractiveness of LES for noise prediction. However, LES has not been applied widely to the tip vortex problem yet. The recent studies by Fleig et al.,[9,10] Cai et al.,[11] Ghias et al.,[12] and Imamura et al.[13] are some of the first applications of LES to the tip vortex problem. The presence of large flow gradients within the boundary layer over the tip surface, as well as in the tip vortex vicinity and the near-field wake, requires sufficiently small grid spacings within these crucial regions so that the separation of the boundary layer followed by a roll up into a vortex and the complex vortex dynamics are accurately captured. The resulting computational grids needed in the LES of a tip vortex may easily reach a size that is on the order of tens of millions of points or even larger. Such substantial resolution requirements have perhaps stood in the way of expansive application of LES to the tip vortex problem. To give the reader a sense of the grid resolution needed, Cai et al.[11] used a grid of 25 million points for the LES of a tip vortex around a NACA0012 wing geometry with a rounded tip, whereas the LES by Ghias et al.[12] used more than 12 million grid points for the computation of the tip vortex around a NACA2415 wing geometry with a blunt tip. Both groups have reported their preliminary results in recent publications. Imamura et al.[13] used 5.9 million grid points for the hybrid LES/RANS calculation of the flow and tip vortex around a rectangular NACA0012 wing with a blunt tip. They performed the LES only in the tip region and switched to RANS in the wing root region. The switching between LES and RANS was done gradually by means of a linearly varying weight function. The LES studies by Fleig et al.[9,10] employed a grid consisting of 300 million grid points for the computation of the tip vortex and the flow around an entire wind turbine blade, even though their main goal was to only study the tip vortex noise. In contrast, the LES by Cai et al.,[11] Ghias et al.,[12] and Imamura et al.[13] consider the spanwise portion of the wing geometry that extends only several chord lengths from the tip region toward the root. Their approach appears to be more economical than that by Fleig et al.[9,10] Also note here that only the studies by Fleig et al.[9,10] and Imamura et al.[13] focus on the noise aspect of this problem, whereas the other LES studies are concerned with turbulence simulation only. Fleig et al.[9,10] performed noise calculations for a wind-turbine blade with two different tip shapes and compared the far-field noise spectra from the two cases to demonstrate the impact of the blade tip design on far-field noise. Although their simulation parameters matched an acoustic experiment of a wind-turbine blade, no comparison of the LES noise prediction results with the experiment has been presented in their publications. Hence, no conclusion can be made regarding the reliability of their LES noise prediction relative to the experiment. On the other hand, Imamura et al.[13] compared the surface pressure spectra with the experiment they simulated and obtained promising results with LES.

The application of LES to tip vortex noise prediction is still in its infancy, and there is much room for growth in this area. The LES calculations by Fleig et al.,[9,10] which are intended for the study of tip vortex noise, employ a third-order upwind scheme for the computation of spatial derivatives in the governing equations. This scheme requires on the order of 30 grid points[9,10] to resolve an acoustic wave accurately. Such a resolution requirement translates into a hefty price tag if one intends use this upwind scheme to compute accurately noise generation and propagation in a three-dimensional problem. Moreover, the inherent numerical dissipation built into the upwind schemes might have an adverse impact on the turbulence as well as the noise field.[14] The sound field is typically several orders of magnitude smaller than the aerodynamic field, and compact finite difference schemes are known to satisfy the strict requirements of CAA while providing adequate wave resolution with typically less than 10 grid points per wavelength.[15,16] The high-order accuracy provided by compact schemes helps reduce the grid resolution requirement and, hence, the overall computational cost. Therefore, the main goal of this research is to perform tip vortex LES with high-order accuracy and use such high-quality numerical solutions to study the tip vortex noise problem. This paper reports on a tip vortex simulation performed by a multiblock LES code that

is based on a compact finite difference scheme and that also has overset grid capability. Data of mean flow and turbulence statistics in the near field of the tip vortex are compared with experimental data. Computation of the tip vortex noise using the near-field LES data is left for future work.

II. Computational Methodology

In this study, the Favre-filtered, unsteady, compressible, nondimensional Navier–Stokes equations formulated in curvilinear coordinates, which are expressed in the following conservative form, are solved:

$$\frac{\partial \boldsymbol{Q}}{\partial t} = -\left[\frac{\partial}{\partial \xi}\left(\frac{\boldsymbol{F}-\boldsymbol{F}_v}{J}\right) + \frac{\partial}{\partial \eta}\left(\frac{\boldsymbol{G}-\boldsymbol{G}_v}{J}\right) + \frac{\partial}{\partial \zeta}\left(\frac{\boldsymbol{H}-\boldsymbol{H}_v}{J}\right)\right] \tag{1}$$

Here, ξ, η, and ζ are the generalized curvilinear coordinates of the computational space and J is the Jacobian of the coordinate transformation from the physical domain to the computational domain. $\boldsymbol{Q} = Q/J$, where $Q = [\bar{\rho}, \bar{\rho}\tilde{u}, \bar{\rho}\tilde{v}, \bar{\rho}\tilde{w}, \tilde{e}_t]^T$, is the vector of conservative flow variables; $\boldsymbol{F}$, $\boldsymbol{G}$, and $\boldsymbol{H}$ are the inviscid flux vectors; and $\boldsymbol{F}_v$, $\boldsymbol{G}_v$, and $\boldsymbol{H}_v$ are the viscous flux vectors. The details of the governing equations can be found in Ref. 17. For simulations of flows around rotating blades, the governing equations should be solved in a rotating frame of reference. The governing equations given in Eq. (1) are valid in an inertial reference frame. One can obtain the governing equations in a noninertial reference frame by adding the following source term to the right-hand side of Eq. (1):

$$\boldsymbol{S} = \frac{1}{J}\begin{bmatrix} 0 \\ \boldsymbol{h}\cdot\boldsymbol{i} \\ \boldsymbol{h}\cdot\boldsymbol{j} \\ \boldsymbol{h}\cdot\boldsymbol{k} \\ \boldsymbol{h}\cdot\boldsymbol{u} \end{bmatrix} \tag{2}$$

where the vector $\boldsymbol{u}$ is the fluid velocity relative to the noninertial system, that is, the rotating blade in our case:

$$\boldsymbol{u} = \tilde{u}\boldsymbol{i} + \tilde{v}\boldsymbol{j} + \tilde{w}\boldsymbol{k} \tag{3}$$

$$\boldsymbol{h} = -\bar{\rho}\left[\frac{\mathrm{d}^2\boldsymbol{R}}{\mathrm{d}t^2} + \frac{\mathrm{d}\boldsymbol{\Omega}}{\mathrm{d}t}\times\boldsymbol{r} + \boldsymbol{\Omega}\times(\boldsymbol{\Omega}\times\boldsymbol{r}) + 2\boldsymbol{\Omega}\times\boldsymbol{u}\right] \tag{4}$$

Here, $\bar{\rho}$ is the fluid density; $\boldsymbol{R}$ and $\boldsymbol{\Omega}$ are the displacement and angular velocity vectors of the noninertial system relative to the inertial system, respectively; and $\boldsymbol{r}$ is the displacement relative to the noninertial system. The functions $\boldsymbol{R}(t)$ and $\boldsymbol{\Omega}(t)$ relate the two systems. In the case of rotation only, that is, no translation, both the first and the second time derivatives of $\boldsymbol{R}$ become zero, and the first term on the right-hand side of Eq. (4) equals zero. The second term also equals zero if $\boldsymbol{\Omega}$ does not vary in time. This paper will present a simulation performed around a nonrotating wing geometry; hence, the source term $\boldsymbol{S}$ is currently set to zero.

A single-block LES code that was previously developed[17−19] has been extended to a multiblock version in this study. Gaitonde and Visbal[20] as well as Visbal and Gaitonde[15] have investigated multiblock implementation strategies in which high-order compact schemes are simultaneously employed in every subdomain and in which grid point overlaps are used to exchange data between adjacent sub-domains during the course of the computations. The attractiveness of this technique is that it allows high-order accurate simulations to be performed in complex domains using multiblock structured grids. A multiblock implementation strategy similar to that by Gaitonde and Visbal[20] is incorporated in the multiblock version of the LES code with a seven-point grid overlap between neighboring blocks. The standard message passing interface library routines have been used in the code parallelization.

We now consider an individual block of the multiblock grid. The nonuniformly spaced curvilinear grid in physical space is transformed to a uniform grid in computational space, and the discretized governing equations are solved on the uniform grid. High-order compact finite difference schemes are used to compute the spatial derivatives in the governing equations. The fourth-order optimized prefactored compact schemes recently developed by Ashcroft and Zhang[16] offer improved dispersion characteristics compared to the standard sixth- and eighth-order compact schemes.[21] The prefactorization strategy splits the central implicit schemes into forward and backward biased operators. The prefactored optimized schemes require the solution of two independent bidiagonal matrices. The spatial derivative at a given grid point i is given by

$$D_i = \tfrac{1}{2}\left(D_i^F + D_i^B\right) \tag{5}$$

where D_i^F and D_i^B represent the forward and backward operators, respectively. The prefactored compact scheme we use is a fourth-order scheme with a five-point stencil. Hence, the forward and backward operators are given as follows:

$$\tfrac{1}{2}D_i^F = (1/2\beta\Delta\xi)[b(f_{i+1} - f_i) + d(f_{i-1} - f_i) + e(f_{i-2} - f_i)]$$
$$\quad - (\alpha/2\beta)D_{i+1}^F \tag{6}$$

$$\tfrac{1}{2}D_i^B = (1/2\beta\Delta\xi)[b(f_i - f_{i-1}) + d(f_i - f_{i+1}) + e(f_i - f_{i+2})]$$
$$\quad - (\alpha/2\beta)D_{i-1}^B \tag{7}$$

where the coefficients α, β, b, d, and e are given by Ashcroft and Zhang[16]; f_i denotes the value of f (the quantity whose spatial derivative is being computed) at grid point i; and $\Delta\xi$ is the uniform grid spacing along a given spatial direction in the computational space. The preceding scheme is applicable to grid points $i = 3$ through $i = N - 2$, where N is the number of grid points along the spatial direction. Additional boundary stencils are required at grid points $i = 1, 2$ and $i = N - 1, N$. The third-order boundary stencils we use are given by Ashcroft and Zhang.[16] At grid points $i = 2$ and $i = N - 1$, the following explicit backward and forward stencils are used:

$$D_2^B = \frac{1}{\Delta\xi}\sum_{i=1}^{4} s_i f_i, \qquad D_{N-1}^B = \frac{1}{\Delta\xi}\sum_{i=N-3}^{N} e_i f_i \tag{8}$$

$$D_2^F = \frac{1}{\Delta\xi}\sum_{i=1}^{4} -e_{N+1-i} f_i, \qquad D_{N-1}^F = \frac{1}{\Delta\xi}\sum_{i=N-3}^{N} -s_{N+1-i} f_i \tag{9}$$

The coefficients $s_i (i = 1, \ldots, 4)$ and $e_i (i = N-3, \ldots, N)$ are given by Ashcroft and Zhang.[16] At grid points $i = 1$ and $i = N$, the following one-sided explicit schemes are employed to compute the spatial derivative:

$$D_1 = \frac{1}{\Delta\xi}\sum_{i=1}^{4} c_i f_i, \qquad D_N = \frac{1}{\Delta\xi}\sum_{i=N-3}^{N} -c_{N+1-i} f_i \tag{10}$$

where $c_1 = -33/18$, $c_2 = 3$, $c_3 = -3/2$, and $c_4 = 1/3$.

The viscous stress terms appearing in the governing equations are obtained using the first derivatives of the velocity components. The spatial derivatives of the inviscid and viscous flux vectors are computed using the prefactored optimized compact scheme. As a consequence of such an implementation, the second derivatives in the viscous fluxes are essentially evaluated by the application of the first-derivative operator twice. Although this approach is not as accurate as when a compact scheme is used to compute directly the second derivatives in the viscous terms, it is much cheaper to implement in curvilinear coordinates. Also note that, for computational efficiency, the terms in the inviscid and viscous fluxes can be added together, and then the total flux can be differentiated. However, the characteristic-type boundary conditions implemented on solid walls (to be discussed shortly) require the separation of inviscid and viscous fluxes; hence, we compute the inviscid and viscous flux derivatives separately in this work.

The LES code also employs the following sixth-order tridiagonal spatial filter used by Visbal and Gaitonde[15]:

$$\alpha_f \bar{f}_{i-1} + \bar{f}_i + \alpha_f \bar{f}_{i+1} = \sum_{n=0}^{3} \frac{a_n}{2}(f_{i+n} + f_{i-n}) \qquad (11)$$

where $\bar{f}_i$ denotes the filtered value of quantity f at grid point i and

$$a_0 = 11/16 + 5\alpha_f/8, \qquad a_1 = 15/32 + 17\alpha_f/16$$

$$a_2 = -3/16 + 3\alpha_f/8, \qquad a_3 = 1/32 - \alpha_f/16 \qquad (12)$$

The parameter α_f must satisfy the inequality $-0.5 < \alpha_f < 0.5$. A less dissipative filter is obtained with higher values of α_f within the given range. With $\alpha_f = 0.5$, there is no filtering effect because Eq. (11) reduces to an identity.

Because this filter has a seven-point right-hand-side stencil, it obviously cannot be used at near-boundary points. Instead, the following sixth-order equation with a one-sided right-hand-side stencil is used at grid points near the left boundary point $i = 1$:

$$\alpha_f \bar{f}_{i-1} + \bar{f}_i + \alpha_f \bar{f}_{i+1} = \sum_{n=1}^{7} a_{n,i} f_n, \qquad i = 2, 3 \qquad (13)$$

where the coefficients $a_{n,i}$ are given by Visbal and Gaitonde.[15] For the points near the right boundary point $i = N$, we apply a similar formulation.[15] The boundary points $i = 1$ and $i = N$ are left unfiltered.

The filtering process eliminates the spurious high-frequency numerical oscillations and ensures numerical stability. Numerical tests show that values of the filtering parameter α_f between 0.45 and 0.49 effectively eliminate the spurious oscillations while providing very little dissipation and, hence, leaving the well-resolved scales mostly unaffected. A value of $\alpha_f = 0.47$, which is in the middle of this range, has been used in the present simulation.

Time advancement can be performed by means of either the standard fourth-order, four-stage explicit Runge–Kutta scheme or a second-order Beam–Warming[22] type implicit time integration scheme (see Ref. 23). The iterative form of the approximately factored finite difference algorithm by Beam and Warming that is second-order accurate in time can be represented as

$$\left[I + \frac{2\Delta t}{3} \frac{\partial}{\partial \xi} \left(\frac{\partial F}{\partial Q} - \frac{\partial F_v}{\partial Q} \right) \right]^p \times \left[I + \frac{2\Delta t}{3} \frac{\partial}{\partial \eta} \left(\frac{\partial G}{\partial Q} - \frac{\partial G_v}{\partial Q} \right) \right]^p$$

$$\times \left[I + \frac{2\Delta t}{3} \frac{\partial}{\partial \zeta} \left(\frac{\partial H}{\partial Q} - \frac{\partial H_v}{\partial Q} \right) \right]^p \Delta Q^p$$

$$= -\left[Q^p - \frac{4}{3}Q^n + \frac{1}{3}Q^{n-1} \right] - \frac{2\Delta t}{3} \left[\frac{\partial}{\partial \xi}(F - F_v) \right.$$

$$\left. + \frac{\partial}{\partial \eta}(G - G_v) + \frac{\partial}{\partial \zeta}(H - H_v) + S \right]^p \qquad (14)$$

I represents the identity matrix, Δt is the time step, and $\Delta Q^p = Q^{p+1} - Q^p$. For $p = 1, Q^p = Q^n$, where n represents the current time level and $n - 1$ represents the preceding time level. Q^{p+1} is the $p + 1$ approximation to the solution at the $n + 1$ time level, Q^{n+1}. Through several subiterations at each time step, ΔQ^p converges toward zero. A second-order-accurate, three-point scheme is used to calculate the time derivative on the right-hand side of Eq. (14). It is well-known that although the Beam–Warming scheme is unconditionally stable in two dimensions, it becomes unstable in three dimensions. To stabilize conditionally the scheme for the three-dimensional computations, we make use of artificial dissipation[24] in the implicit side of Eq. (14). For example, while applying the

equation along the ξ direction, the artificial dissipation operator is appended to the implicit operator, as follows:

$$\left[I + \frac{2\Delta t}{3} \frac{\partial}{\partial \xi} \left(\frac{\partial F}{\partial Q} - \frac{\partial F_v}{\partial Q} \right) \right.$$

$$\left. - \epsilon_I \nabla_\xi \left(\sigma_{i+1,j,k} J_{i+1,j,k}^{-1} + \sigma_{i,j,k} J_{i,j,k}^{-1} \right) \Delta_\xi J \right]^p \qquad (15)$$

where $\nabla_\xi f_{i,j,k} = f_{i,j,k} - f_{i-1,j,k}$, $\Delta_\xi f_{i,j,k} = f_{i+1,j,k} - f_{i,j,k}$, $\sigma_{i,j,k}$ is the spectral radius of the inviscid flux Jacobian ($\partial F/\partial Q$) at grid point (i, j, k), J is the Jacobian of the coordinate transformation, and ϵ_I controls the strength of the artificial dissipation. Through numerical experimentation, $\epsilon_I = 0.5\Delta t$ was found to provide adequate artificial dissipation to maintain stability in the present calculations. For the relatively high Reynolds numbers considered in this study, the contribution of the viscous flux Jacobians, $\partial F_v/\partial Q$, $\partial G_v/\partial Q$, and $\partial H_v/\partial Q$ to the left-hand side of Eq. (14) can be considered negligible because the viscous flux Jacobians are normalized by the Reynolds number. Hence, the somewhat cumbersome evaluation of the viscous flux Jacobians in generalized curvilinear coordinates is skipped in this work. The spatial derivatives operating on the fluxes on the right-hand side are computed using the prefactored optimized compact scheme described earlier. On the other hand, the spatial derivatives operating on the flux Jacobians on the left-hand side are computed using the fourth-order compact scheme by Lele.[21] Use of compact schemes to attain high-order spatial accuracy for the implicit operators was originally proposed by Ekaterinaris.[23] The implicit time-stepping algorithm we have implemented then becomes truly second-order accurate in time and fourth-order accurate in space. Application of compact schemes for the implicit operators results in a block tridiagonal matrix system along each of the three computational directions, which are solved sequentially as described by Ekaterinaris.[23] This procedure basically replaces the three-dimensional problem by three one-dimensional problems at a given time level. Numerical experiments have shown that typically two or three subiterations per time step are sufficient to reduce the errors due to approximate factorization, linearization, and artificial dissipation and, consequently, drive ΔQ^p toward zero at each time step. The solution is filtered after every subiteration to ensure numerical stability.

Tam and Dong's radiation boundary conditions[25] are applied on the boundaries to which only acoustic disturbances are reaching. The original two-dimensional boundary conditions of Tam and Dong were extended to three-dimensions by Bogey and Bailly.[26] Inflow boundaries can be handled by either characteristic-type inflow boundary conditions[27] or Tam and Dong's radiation boundary conditions. For the boundaries that entropy, vorticity, and acoustic waves are crossing, Tam and Dong's outflow boundary conditions are used. We additionally attach a sponge zone downstream of the physical domain and apply grid stretching in combination with artificial damping in this region to dissipate the turbulence in the flowfield before it reaches the outflow boundary. This way, unwanted numerical reflections from the outflow boundary are suppressed. On solid walls, a generalized characteristic-type solid wall boundary condition[28] is applied. The wall temperature is computed using either isothermal or adiabatic boundary conditions. Application of the boundary conditions when explicit time stepping is used is straightforward. In this case, on the boundary points, the residual on the right-hand side of Eq. (1) is simply overwritten by the boundary conditions. In the case of implicit time stepping on the boundary points, the sum of the flux derivatives appearing on the right-hand side of Eq. (14) is replaced by the boundary conditions. Moreover, when solid wall boundaries are present, the block tridiagonal system of equations must be modified such that all velocity components on viscous walls are enforced to be zero, whereas, on inviscid walls, only the velocity component normal to the wall is enforced to be zero.

At every time step, the solution is advanced independently in each block. Information is exchanged among the blocks at the end of each stage of the Runge–Kutta time integration scheme or after

every subiteration of the implicit time integration scheme, as well as after each application of the filter.

No explicit subgrid-scale (SGS) model is used in the present LES calculations. Instead, the spatial filter implemented in the LES is treated as an implicit SGS model. It is well understood regarding turbulent flows that the energy cascade is associated with a mean flux of energy that is directed from large scales toward small scales. The large scales contain the major part of the turbulent kinetic energy, and they continuously feed the turbulent kinetic energy via the cascade to the smallest eddies where it is dissipated. Because the grid resolution is too coarse to resolve all of the relevant length scales in an LES, the pile up of energy at the high wave numbers can be eliminated through the use of a spatial filter. Hence, the spatial filter can be thought of as an effective SGS model in an LES. Visbal and Rizzetta[29] and Visbal et al.[30] have performed LES calculations of turbulent channel flow and compressible isotropic turbulence decay without using any explicit SGS model. In those simulations, spatial filtering was treated as an implicit SGS model. They also showed that the use of an SGS model, such as the dynamic Smagorinsky model, in those simulations did not produce results superior to those obtained without employing an explicit SGS model. The use of the popular dynamic Smagorinsky model in an LES can increase the computational cost by up to 50% (Ref. 17). Moreover, recent studies about the impact of the Smagorinsky model on jet noise calculations (see Refs. 17 and 31) showed that the eddy viscosity of the model can have undesirable effects on noise prediction. This continues to be an unresolved issue, and, consequently, it was decided not to employ the dynamic Smagorinsky model in the present computations.

We have also implemented overset grid capability into our multi-block LES code. The overset grid approach (also known as Chimera; see, for example, Benek et al.[32]) provides added flexibility in meshing domains around complex geometries and is useful for avoiding grid point singularities. For example, if one tries to generate a single surface grid over a wing with a rounded tip, a grid point singularity may arise at the point where the trailing edge of the tip joins the trailing edge of the wing. The overset grid approach can easily avoid such singularity problems. In this study, a separate tip cap grid is generated around the tip and another grid is generated around the main wing surface (excluding the tip region).

The overset grid approach consists of individual component grids generated around each geometric feature of interest (such as the main wing or wind-turbine blade surface and the tip geometry, in our case) and a background grid in which all of the individual components are embedded. The component grids may cut holes in the background grid and in other component grids to remove the excess grid overlap. Holes also allow grids containing solid surfaces to be embedded in background grids. Hole cutting in the present work is accomplished by means of the OGEN program[33] developed at the Lawrence Livermore National Laboratory. An intermediate program reads in the output of OGEN and reorganizes the data for use with our LES code. Special bookkeeping is required in the LES code to keep track of the hole points.

In the overset grid approach, the points in the overlapping regions between grid components are not coincident. Hence, interpolation is necessary to exchange information between neighboring component grids during the course of the computations. It was previously shown by Sherer and Scott[34] that the use of second-order interpolation at grid boundaries results in a globally second-order accurate solution, even when high-order compact differencing and filtering are used. Hence, we employ sixth-order-accurate explicit Lagrangian interpolation in this work in conjunction with the high-order compact differencing and filtering schemes implemented in our code to ensure that a high-order-accurate numerical solution is maintained throughout the entire computational domain. The sixth-order interpolation stencils are precomputed by the OGEN code. The three-dimensional interpolation stencil consists of seven points along each of the three computational coordinate directions. The interpolation process takes place in the computational space. Also note that OGEN computes the location of the interpolation points within the computational space of a donor grid with only second-order accuracy. If sixth-order accuracy is desired in the interpolation

process, then the location of the interpolation points within the computational space must be determined with sixth-order accuracy as well. For this purpose, a preprocessing program makes use of the interpolation stencils given by OGEN and computes the location of the interpolation points with sixth-order accuracy using a procedure described by Sherer[35] and Sherer and Scott.[34]

Another challenging aspect of the overset grid approach is that once all of the component grids are partitioned into smaller blocks for parallel computing, the number of grid points per block can vary greatly. Hence, load balancing during the course of parallel computing becomes an important issue. One way to ensure good load balancing is to assign multiple blocks per processor so that each processor works on roughly the same number of grid points. Hence, we have modified our code so that it can handle multiple blocks per processor. The component grids are partitioned so that the total number of blocks is at least equal to twice the number of processors available. Then, the blocks are distributed to the processors such that the total number of grid points per processor is approximately equal.

Far-field noise computations can be performed by coupling the time-accurate, unsteady near-field data provided by the LES either with the Ffowcs Williams–Hawkings method (see Ref. 19) or with a linearized Euler solver. The acoustic calculations via the Ffowcs Williams–Hawkings method require very little further effort after the unsteady flowfield has been computed by the LES because only the surface integrals in the Ffowcs Williams–Hawkings formulation need to be evaluated. The quadrupole volume integral appearing in the Ffowcs Williams–Hawkings formulation is not expected to be a significant contributor to the far-field noise as long as the flow Mach number is low (see Ref. 36). In this paper, the main emphasis is to compare the numerical results with the mean flow and turbulence measurements in the near field of a wing tip vortex that was experimentally studied by Chow et al.[1,37] Computation of the tip vortex noise is, therefore, left for future work.

III. Test Case: Vortex Formation Around Rounded Tip Geometry

A. Simulation Details

We present results from the simulation of an experimental test case previously studied by Chow et al.[1,37] The computational configuration is shown in Fig. 2. In this test case the tip vortex formation around a nonrotating wing with a rounded tip is studied. The wing cross section has the NACA0012 airfoil geometry. The ratio of the wing span (including the tip) b to the chord c is 0.75. The model is mounted on the side wall of the wind-tunnel test section as shown in Fig. 2. The model is rotated about the quarter-chord axis to adjust the freestream angle of attack. The freestream flow approaches the wing model at a Mach number of approximately 0.15 and an angle of attack of 10 deg. The Reynolds number, based on the freestream velocity, freestream kinematic viscosity, and wing chord length, Re_c, is about 4.6×10^6 in the experiment; however, we set the Reynolds number to half a million in the LES to keep the resolution requirements of the simulation at an acceptable level. The implication of using a Reynolds number that is about an order of magnitude smaller than that of the experiment will be discussed when the LES results are compared with the experiment. Another difference between the
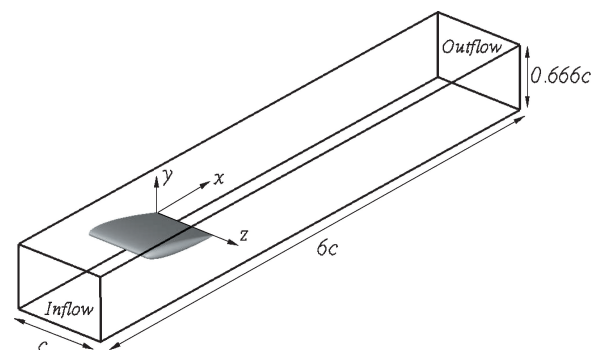

Fig. 2 Schematic showing wing model in wind tunnel.

experiment and the LES is that the boundary layers are tripped near the wing leading edge in the experiment, whereas in the LES, we allow the boundary layers to transition naturally to turbulence as the numerical implementation of boundary-layer tripping is not an easy and straightforward task.

There are three component grids in this simulation. The first one is the tip cap grid that is generated around the tip of the wing geometry. The second component grid is the one that is generated around the main surface of the wing geometry. The third one is the background grid in which the wing grid and the tip cap grid are embedded. The background grid represents the wind tunnel. The tip cap grid cuts holes in both the wing grid and the background grid. The wing grid also cuts holes in the background grid. All lengths are nondimensionalized by a reference length scale that is taken as the constant wing chord length, c. The x direction is taken as the streamwise direction, whereas y is the vertical direction and z is the spanwise direction. The origin of the xyz coordinate system is attached to the wing root trailing edge as shown in Fig. 2. The background grid starts at about one chord upstream of the wing leading edge and ends at about four chord lengths downstream of the trailing edge. The tunnel width is equal to one chord length, whereas the tunnel height is $0.666c$. The vertical distance between the quarter-chord axis of the wing geometry and the upper or lower tunnel wall is $0.333c$. The physical portion of the background grid ends at about one chord length downstream of the trailing edge. The sponge zone, which is another three chord lengths, damps out the turbulence in the flowfield before it reaches the outflow boundary. The sponge zone contains only about 15% of the grid points along the streamwise direction. The root of the wing geometry coincides with the side of the background grid on the $z/c = 0$ plane. Inviscid wall boundary conditions are applied on all tunnel walls to reduce the grid resolution requirements normal to the tunnel walls. Moreover, a symmetry plane boundary condition is additionally imposed on the tunnel wall that coincides with the wing root. For the background grid, characteristic-type inflow boundary conditions are applied on the inlet plane, whereas Tam and Dong's[25] outflow boundary conditions are applied on the exit boundary. Viscous wall boundary conditions are applied on the faces of the tip cap grid and the wing grid that coincide with the wing and tip geometry surfaces. All of the other faces of these two grids, other than the face of the wing grid on the $z/c = 0$ plane (inviscid wall), are interpolation boundaries. Finally, adiabatic boundary conditions are applied on all walls. Although temperature is not one of the solution variables, it is related to density and pressure through the ideal gas relation. Adiabatic wall boundary conditions are enforced by setting the heat flux term in the wall normal direction to zero in the energy equation.

Table 1 provides various information about the component grids that make up the overset grid topology in this test case. The grid points column shows the total number of grid points in every component grid prior to hole cutting. The interpolation points column shows the total number of interpolation points, and the unused points column gives the number of unused points after hole cutting is done by OGEN.[33] The last column shows the number of blocks into which every component block has been partitioned. The total number of grid points at which the governing equations must be solved is equal to approximately 26.2 million. The three component grids are partitioned into 256 blocks total. The blocks are distributed to 124 processors such that the total number of grid points per processor is approximately equal. This ensures a good load balance among the processors during the course of parallel computations.

Figure 3 shows the overset grid topology on the wing and tip geometry surfaces. The black grid shows the discretization on the
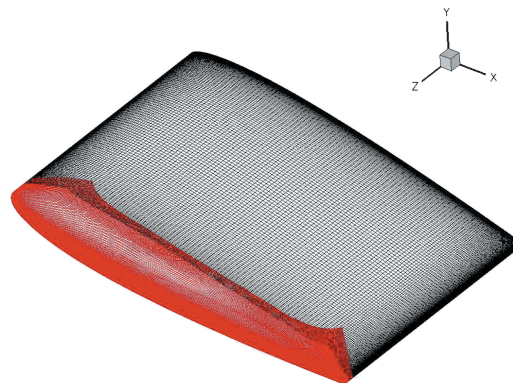

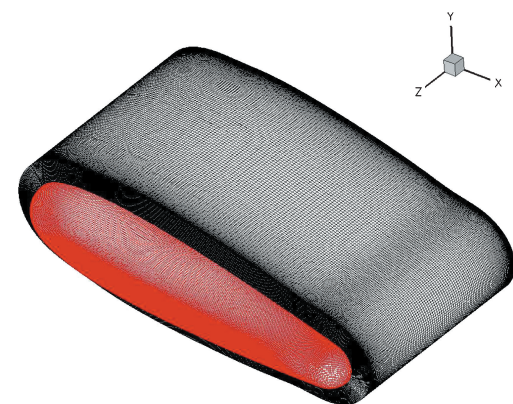**Fig. 3   Overset grids on wing and tip geometry surfaces.**

Fig. 4   Volume overset grids.

main surface of the wing geometry, whereas the red one shows the one on the rounded tip. The tip cap grid wraps smoothly around the tip geometry. The grid around the main wing surface is an O grid. By using the overset grid topology shown here, we avoid grid point singularities. Figure 4 shows the volume overset grids. Both of these volume grids are embedded in the background grid, as mentioned earlier.

In the background grid, both the vertical and spanwise grid spacing inside and around the tip vortex is slightly less than $3 \times 10^{-3}c$. The portion of the background grid in this region is fairly uniform with an aspect ratio of about one. Immediately downstream of the trailing edge, the streamwise spacing in the background grid is about $4 \times 10^{-3}c$ and increases to a value of $3 \times 10^{-2}c$ by the end of the physical domain. In the sponge zone, the streamwise spacing is stretched from $3 \times 10^{-2}c$ to $2.5 \times 10^{-1}c$ using a total of 48 grid points. Normal to the wing and tip surfaces, the grid spacing is about $7.5 \times 10^{-5}c$. Accurate estimation of the wall normal grid spacing in terms of wall units is difficult without a priori knowledge of the wall shear stresses. However, using the mean wall shear stress data obtained from the simulation, it was determined that along the upper side of the wing geometry, where the tip vortex and wing surface interaction occurs, the normal grid spacing in terms of wall units, $\Delta W^+ = \Delta W u_\tau / \nu$, reached a maximum value of around three. Preliminary estimations using flat-plate skin-friction correlations, on the other hand, had provided a value of around 1.5 or 2. No near-wall modeling was used in the present calculation. In the tip cap grid, where the tip vortex originates, the coarsest normal grid spacing away from the wall is on the order of $1.86 \times 10^{-3}c$. The coarsest spanwise or streamwise grid spacing in the tip cap surface grid is about two orders of magnitude larger than the wall normal spacing. The same is true for the wing surface grid. The grid spacing normal to the tunnel wall at the wing root is $2.5 \times 10^{-4}c$, whereas it is $5 \times 10^{-3}c$ at the other three tunnel walls. Recall that all tunnel walls are treated as inviscid walls in the simulation.

The simulation was performed with implicit time stepping and was run in several stages. Two subiterations were applied per

Table 1   Grid information

Component grid	Grid points	Interpolation points	Unused points	Blocks
Background	16,000,000	415,207	2,730,946	144
Wing	8,379,000	391,827	512,276	80
Tip cap	5,027,400	412,140	0	32
Total	29,406,400	1,219,174	3,243,222	256

time step. The filtering parameter was set to $\alpha_f = 0.47$. The first 13,350 time steps were run with a maximum Courant–Friedrichs–Lewy (CFL) number corresponding to 10. Because the computation proved to be stable at this CFL number, we decided to increase it to 15 for the remainder of the simulation to reduce the total integration time and, hence, the overall simulation cost. Also note here that the maximum CFL number of 15 is the CFL number of the cells next to the viscous wall. Because grid stretching is applied in the wall normal direction, the CFL number drops with increasing distance from the wall. The CFL number is smaller than one for the great majority of the grid cells in the computational domain. With a maximum CFL number of 15, 6667 time steps were required per chord-flow time. The chord-flow time is defined as the timescale required by a fluid particle moving at the freestream velocity to travel one chord length. In other words, it is equal to one nondimensional time unit that is given by the ratio of the wing chord c and the freestream velocity u_∞. When 124 processors are used on an IBM-SP4 machine with POWER4 type processors running at 1.1-GHz speed, about 133 h of run time was needed per chord-flow time (at a maximum CFL number of 15). On the other hand, the code runs 2.5 times faster on the National Computational Science Alliance Xeon Linux Cluster (Tungsten)[38] that utilizes Intel Xeon 3.2-GHz processors. Hence, using 124 processors on Tungsten, about 53 h of run time is needed per chord-flow time. With the maximum CFL number of 15, the computational time step in wall units, $\Delta t^+ = \Delta t u_\tau^2/\nu$, turns out to be about 0.5. It is known that the viscous timescale or the Kolmogorov timescale in the sublayer of a turbulent boundary layer is $\mathcal{O}(1)$ in wall units (see Refs. 39 and 40). Because our coarsest wall normal grid spacing in terms of wall units is around three, we resolve several times the Kolmogorov length scale in the near-wall region. This means that the smallest timescale associated with the smallest length scale resolved in the simulation is several times the Kolmogorov timescale. Hence, we believe that our computational time step is small enough to resolve accurately this smallest timescale of turbulence in the boundary layer.

Visual analysis of the streamlines depicting the tip vortex, as well as of pressure and streamwise velocity contours in the domain, is helpful in determining the downstream propagation of the initial numerical transients. Even though the streamwise portion of the physical domain extends one chord length downstream of the trailing edge in this test case, during the simulation it was decided to limit our region of interest to $0.5c$ downstream of the trailing edge to reduce the simulation run time and the computation cost. Because the flow Mach number is very low in this test case, it takes about 32,000 time steps for the initial numerical transients to move out of the region of interest that extends to $0.5c$ downstream of the trailing edge. This corresponds to a timescale of about 4.1 chord-flow times. After the numerical transients exit the region of interest, we collect the flow statistics over a sampling period corresponding to about 5.7 chord-flow times. Hence, the simulation is run for 69,800 time steps total. The first 44,750 time steps of the simulation were run on the IBM-SP4 machine mentioned earlier, and the remainder were completed on Tungsten. If the entire simulation were run on Tungsten, the total computation time would be about 558.4 h or 23.3 days. Although this is a substantial computing cost, the great savings in computing time brought about by the implicit time stepping are worth mentioning at this point. The second-order implicit time-stepping scheme (with two subiterations per time step) we have implemented and used in this simulation is approximately 10/3 times more expensive than the fourth-order, four-stage explicit Runge–Kutta time-stepping scheme. When it is assumed that the same simulation could be performed with the explicit time stepping using a CFL number of 1, the simulation then would be 4.5 times more expensive (relative to the simulation performed using implicit time stepping with CFL number of 15). It is known that on highly stretched meshes, usually a CFL number on the order of 0.5 or smaller must be used with explicit schemes to maintain stability. The same simulation using explicit time stepping with a CFL number of 0.5 would be nine times more expensive. The advantage of using an implicit time stepping in this problem is obvious.

B.   Simulation Results and Comparison with Experiment

Before going into a discussion of the comparison of LES results with the experimental data of Chow et al.,[1,37] we recall the following main differences between the experiment and the LES:

1) In the experiment, the boundary layers are tripped around the wing leading edge, whereas in the LES, the boundary layers are allowed to transition naturally to turbulence because the numerical implementation of boundary-layer tripping is not straightforward. Hence, in the experiment, the boundary layers on the suction side of the wing and the wing tip region become turbulent after the trip, whereas in the LES, the boundary layers reach a turbulent state further downstream.

2) The LES Reynolds number is almost an order of magnitude smaller than that of the experiment.

3) The experimental wing configuration has a sharp trailing edge, whereas the trailing edge of the wing geometry in the LES is rounded because the handling of sharp trailing edges in a numerical computation is somewhat troublesome.

These differences should be kept in mind while analyzing the comparisons between the LES and the experiment. In the following discussion, the effects of the Reynolds number on the tip vortex behavior will be explained whenever appropriate. Yet, it is important to remember that the difference in the initial state of the boundary layers might also be partially responsible for some of the discrepancies that will be observed between the LES results and the experimental measurements.

Figure 5 shows the vortex formation around the rounded tip. The crossflow taking place over the edge of the rounded tip and subsequent vortex formation are shown by means of flow streamlines. Figure 5 is actually the same as Fig. 1 shown earlier, but it shows the vortex formation from a different view angle.

We first examine the location of the vortex core centerline as a function of streamwise distance. As shown in Fig. 2, the origin of the xyz coordinate system is taken as the wing root trailing edge. The crossflow velocity, which is defined as $\sqrt{(\langle\tilde{v}\rangle)^2 + (\langle\tilde{w}\rangle)^2}$, where $\langle\tilde{v}\rangle$ and $\langle\tilde{w}\rangle$ are the time-averaged y and z components of the velocity vector, respectively, approaches zero in the vortex core. Hence, on a given crossflow plane, the vortex core location centerline is determined by the location of the minimum crossflow velocity. Figures 6 and 7 show the y/c and z/c paths of the vortex core, respectively, and make comparisons with the experiment. The trailing edge of the wing is at $x/c = 0$. The first indication of a tip vortex was observed on the $x/c = -0.394$ plane in the experiment and the subsequent measurements were obtained starting from this plane and moving downstream. In the LES, however, we could not identify a well-defined vortex core location on the first two crossflow planes because the LES tip vortex is still in the early stages of roll up and formation on these planes. Hence, we perform the comparisons starting at the $x/c = -0.197$ plane. As is obvious from Figs. 6 and 7,
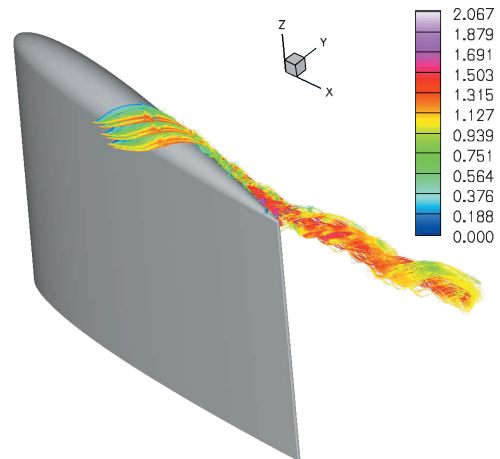

Fig. 5   Streamlines showing formation of tip vortex; colors denote magnitude of instantaneous axial velocity normalized by freestream velocity.
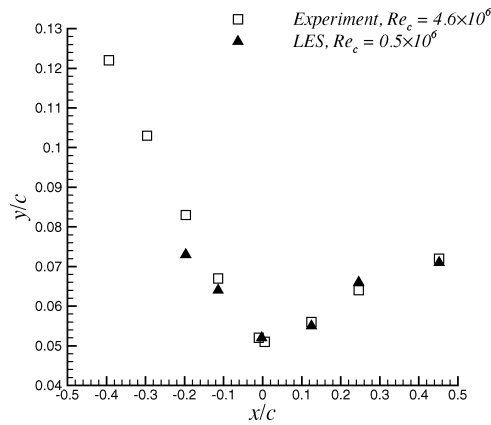
Fig. 6   Path y/c of tip vortex core; trailing edge of wing tip is at $x/c = 0$ and $y/c = 0$.
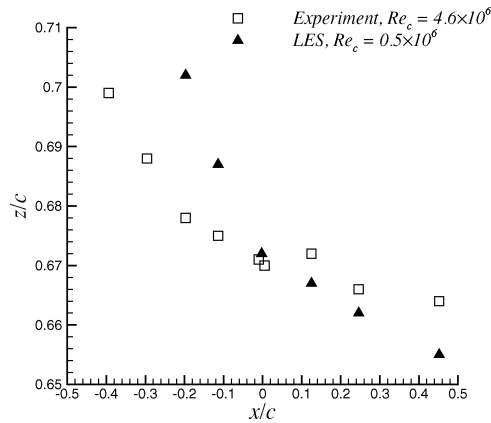

Fig. 7   Path z/c of tip vortex core; trailing edge of wing tip is at $x/c = 0$ and $z/c = 0.69$.

the y/c and z/c paths of the LES vortex core centerline differ from the experiment by some amount on the first two planes of comparison. The difference at these two locations is more pronounced in the z/c path. As will be evident later, the initial roll up of the LES vortex was found to be noticeably different from the experimental vortex. Hence, the differences in the vortex core location on the first two planes is not surprising. Interestingly, by the time the LES vortex reaches the trailing edge, its core location centerline is almost the same as the experimental one. In both cases, before the trailing edge is reached, the y/c path moves downward. Downstream of the trailing edge, in both cases, the vortex moves upward and good agreement between LES and experiment is evident in the y/c path plot. On the other hand, along the spanwise direction, the LES vortex follows an inboard path at all planes. The experimental one shows a similar trend, except at $x/c = 0.125$, where it moves outboard briefly and then resumes its inboard path at the next location. This experimental kink was believed to be due to the absorption of secondary vortices into the primary vortex. In the experiment, it was found that a secondary vortex was induced by the effect of the main vortex on the tip boundary layer. Moreover, a tertiary vortex outboard of the secondary vortex was observed. The rotational sense of the secondary vortex is opposite to that of the primary vortex, whereas the tertiary vortex has the same sense of rotation as the main vortex. Secondary and tertiary vortices were also observed in the LES. Figure 8 shows the streamlines on the crossflow plane at $x/c = -0.114$, which verify the presence of secondary and tertiary vortices in the LES. However, probably due to the lower Reynolds number of the LES, these vortices seem to be very weak, and the lack of the kink in the z/c path of the LES vortex is most probably because these secondary vortices are so weak that their absorption into the main vortex does not alter the spanwise path of the main vortex in a noticeable way. Also note that the inboard movement of the LES vortex downstream of the trailing edge is greater than that
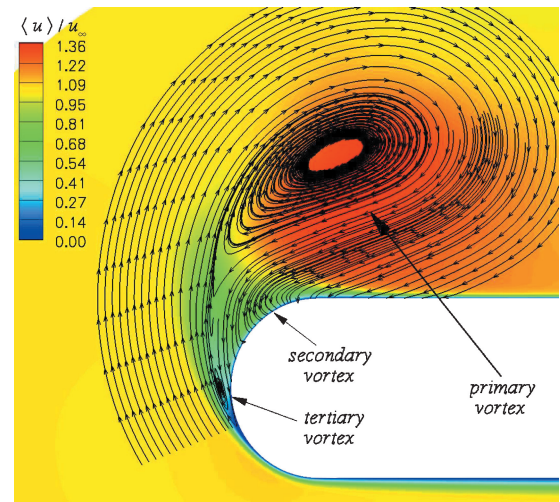

Fig. 8   Streamlines showing primary, secondary, and tertiary vortices on crossflow plane at $x/c = -0.114$; colors denote magnitude of mean axial velocity normalized by freestream velocity.
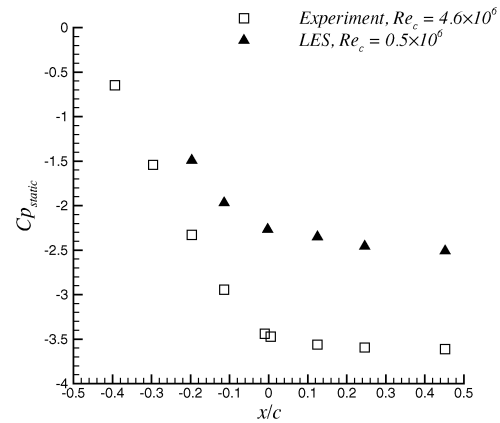

Fig. 9   Negative peak static pressure coefficient along vortex core; trailing edge of wing tip is at $x/c = 0$.

of the experimental vortex. McAlister and Takahashi[41] report that tripping the boundary layer near the leading edge of a NACA0015 wing reduces the inboard movement of the tip vortex along the span, while having no detectable effect on its vertical movement in the wake region. Our comparisons with the data of Chow et al.[1,37] seem to support the observation by McAlister and Takahashi.[41] To reiterate, the boundary layers were tripped near the wing leading edge in the experiment by Chow et al.[1,37] The vertical path of the LES vortex core is almost the same as the experimental one downstream of the trailing edge, whereas the inboard movement of the LES vortex core along the span is clearly greater than that of the experimental vortex. Overall, the y/c and z/c paths of the LES vortex show good overall qualitative agreement with the experiment.

Next, we examine the streamwise variation of the negative peak static and minimum total pressure coefficients along the vortex core. The static and total pressure coefficients are defined as

$$Cp_{\text{static}} = \frac{p - p_\infty}{\frac{1}{2}\rho_\infty u_\infty^2}, \qquad Cp_{\text{total}} = \frac{p_{\text{total}} - p_\infty}{\frac{1}{2}\rho_\infty u_\infty^2} \qquad (16)$$

Inside the vortex core, the static pressure is lower than the freestream pressure. The negative peak static pressure coefficient inside the vortex core at a given crossflow plane quantifies the maximum deviation of the static pressure from the freestream pressure. On the other hand, the minimum total pressure coefficient inside the vortex core at a given crossflow plane quantifies the maximum loss in the total pressure. Figures 9 and 10 show the negative peak static and minimum total pressure coefficient distributions, respectively.
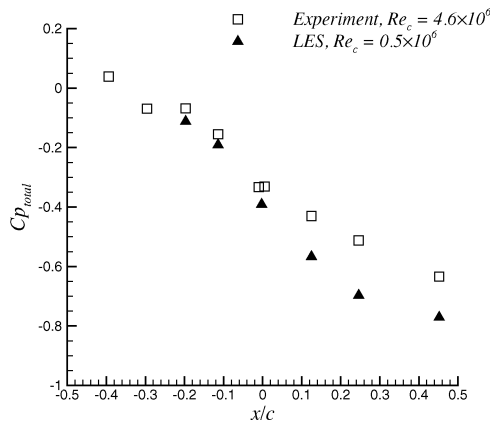
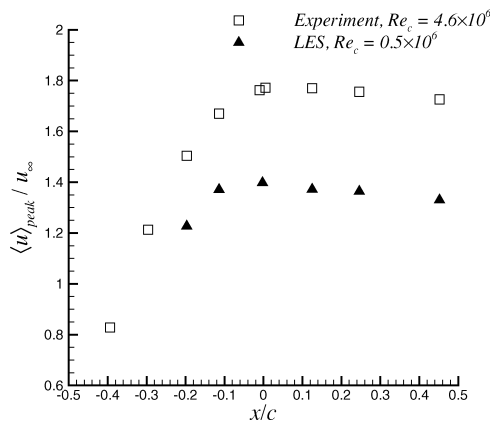Fig. 10   Minimum total pressure coefficient along vortex core; trailing edge of wing tip is at $x/c = 0$.

Fig. 12   Comparison of pressure coefficient distribution over wing surface near wing tip at $z/c = 0.6667$; leading edge of wing surface is at $x''/c = 0$ and trailing edge is at $x''/c = 1$.

Fig. 11   Normalized peak mean axial velocity along vortex core; trailing edge of wing tip is at $x/c = 0$.

Fig. 13   Comparison of pressure coefficient distribution over side edge of tip geometry; leading edge of tip geometry is at $x''/c = 0$ and trailing edge is at $x''/c = 1$.

It is clear from Fig. 9 that a large favorable axial pressure gradient develops upstream of the trailing edge in the experimental vortex core. The static pressure levels off downstream of the trailing edge. The LES vortex core also displays similar behavior; however, the static pressure drop in the LES vortex core is not as severe as the experimental one. It is believed that the lower Reynolds number of the LES is one of the causes for this difference, as will be explained shortly. On the other hand, the total pressure coefficient drop in the LES vortex core is more severe in the planes downstream of the trailing edge, as shown in Fig. 10. Because most of the fluid in the vortex core originates from the detached boundary layers on the tip surface, the total pressure loss inside the vortex core is due to viscous effects. Because the Reynolds number of the LES is an order of magnitude smaller than that of the experiment, the viscous effects in the LES should be more dominant than they are in the experiment. As a result, the total pressure loss in the LES vortex core is more severe than that in the experiment. Stated another way, a lower Reynolds number means that viscosity plays a larger role in the LES than in the experiment. Hence, the low momentum boundary-layer fluid wrapped into the tip vortex is expected to have a larger effect in the LES. Moreover, the lower absolute levels of the static pressure coefficient in the LES vortex core are possibly due to the viscous effects counteracting the favorable pressure gradient forces.

Figure 11 shows a comparison of the peak normalized mean axial velocity along the vortex core. The mean axial velocity in the experiment reaches a peak of almost $1.8u_\infty$ around the trailing edge, whereas the peak value of the LES is around $1.4u_\infty$. The favorable pressure gradient is directly responsible for such high axial velocity excess in the vortex core.[42] Because the axial pressure gradient upstream of the trailing edge in the experiment was higher than that in the LES, the experimental peak axial velocity naturally reaches a higher value. This is again a direct consequence of the
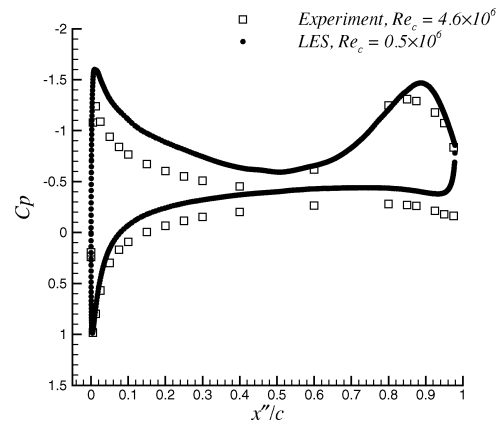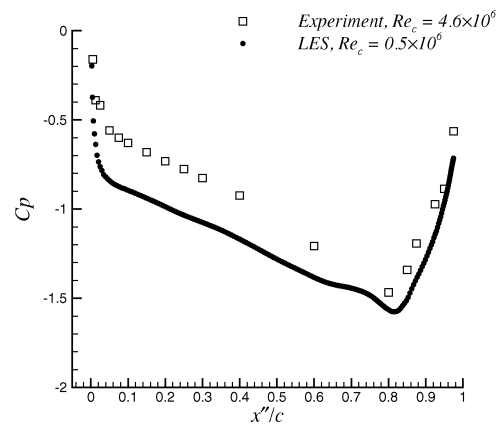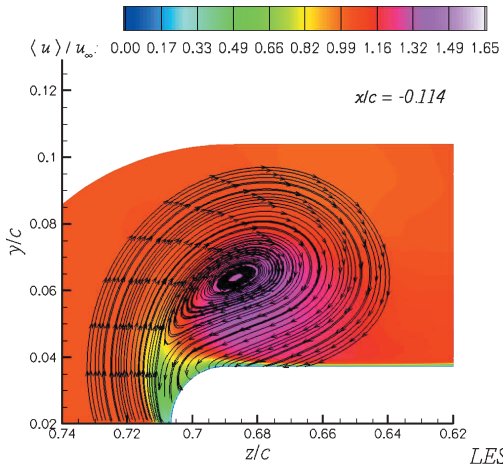
higher Reynolds number. In both cases, the axial velocity decays very slowly downstream of the trailing edge. The core axial velocity downstream of the trailing edge is influenced by parameters such as the tip shape, angle of attack, Reynolds number, and wing aspect ratio. Analyzing their own experimental data and data from numerous other experiments, Chow et al.[1] show that, in general, the peak axial velocity increases with angle of attack and Reynolds number, whereas it decreases with streamwise distance downstream of the trailing edge and wing aspect ratio.

Figure 12 shows a comparison of the pressure coefficient distribution on the wing suction and pressure surfaces at the $z/c = 0.6667$ location that is near the tip. Note that on the viscous surface, $Cp = Cp_{\text{static}} = Cp_{\text{total}}$ because the velocity on the surface is zero. McAlister and Takahashi[41] point out that the pressure distribution near the rounded tip of a NACA0015 wing is influenced by the Reynolds number. Hence, some differences in the surface pressure distribution near the tip should be expected when the present lower Reynolds number LES is compared against the higher-Reynolds-number experiment. Moreover, the difference in the initial state of the LES and experimental boundary layers may also be important for the surface pressure distributions. As can be seen from Fig. 12, the peak near the leading edge on the pressure side of the wing is equal to approximately one in both the LES and the experiment, whereas the suction side peak near the leading edge in the LES is higher than that of the experiment. The secondary peak near the trailing edge on the suction side, which is due to the tip vortex, is predicted reasonably well by the LES when compared to the experiment.

Figure 13 shows the pressure coefficient distributions over the side edge of the rounded tip. The distributions are plotted along a line that cuts the tip geometry in half. Initially, the pressure coefficient
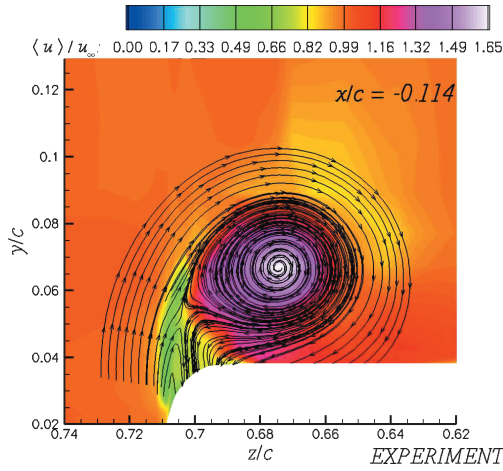
Fig. 14 Experimental streamlines superimposed on normalized mean axial velocity contours on crossflow plane at $x/c = -0.114$. (For peak mean axial velocity on this plane, see Fig. 11.)
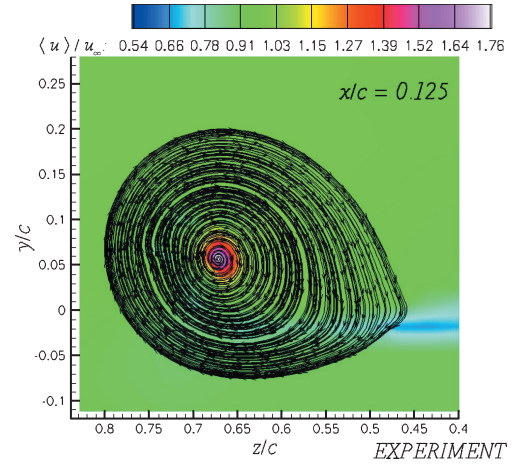

Fig. 15 LES streamlines superimposed on normalized mean axial velocity contours on crossflow plane at $x/c = -0.114$. (For peak mean axial velocity on this plane, see Fig. 11.)

Fig. 16 Experimental streamlines superimposed on normalized mean axial velocity contours on crossflow plane at $x/c = 0.125$. (For peak mean axial velocity on this plane, see Fig. 11.)

Fig. 17 LES streamlines superimposed on normalized mean axial velocity contours on crossflow plane at $x/c = 0.125$. (For peak mean axial velocity on this plane, see Fig. 11.)

Fig. 18 Experimental turbulent kinetic energy contours on crossflow plane at $x/c = -0.114$.

drops very rapidly along this line near the leading edge. This must be due to the acceleration of the flow over the leading-edge portion of the rounded tip. Pressure continues to drop at a reduced rate farther along the line until about $x''/c = 0.8$, where it starts to rise rapidly. Once again, we find good overall qualitative agreement between the LES and the experiment when the surface pressure distributions in the near-tip region and on the tip side edge are compared.
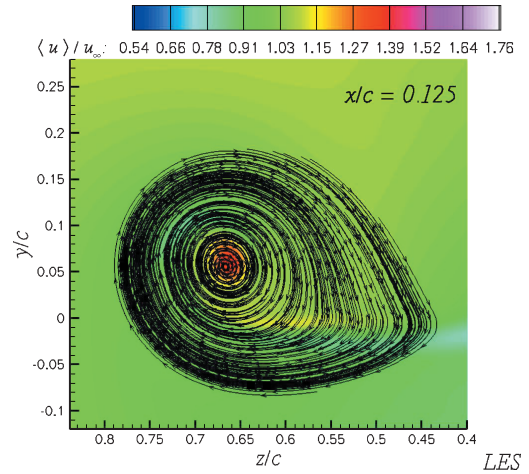
As mentioned earlier, the initial roll-up process of the tip vortex was found to be somewhat different in the LES when compared to the experiment. For example, if we examine the streamlines on a crossflow plane located at $x/c = -0.114$, which is upstream of the trailing edge, we see that the LES vortex structure on this plane is quite different than the experiment. Figures 14 and 15 show this comparison. The experimental vortex is seen to have a circular shape on this crossflow plane, yet the LES vortex displays a skewed pattern. On the other hand, if we look at a crossflow plane downstream of the trailing edge, for example at $x/c = 0.125$, we see that this time the LES vortex structure is quite similar to that of the experimental one, as shown in Figs. 16 and 17. Thus, even though the initial roll up and formation of the two vortices are somewhat different upstream of the trailing edge, the two vortices seem to have a similar structure downstream of the trailing edge.

It is also of interest to examine the turbulent kinetic energy contours to see the differences between the LES and the experiment. The normalized turbulent kinetic energy is defined as
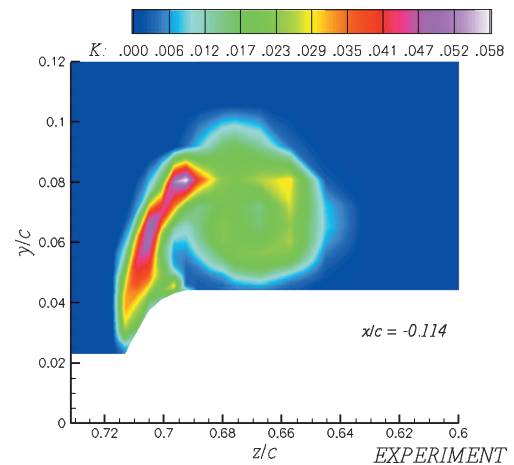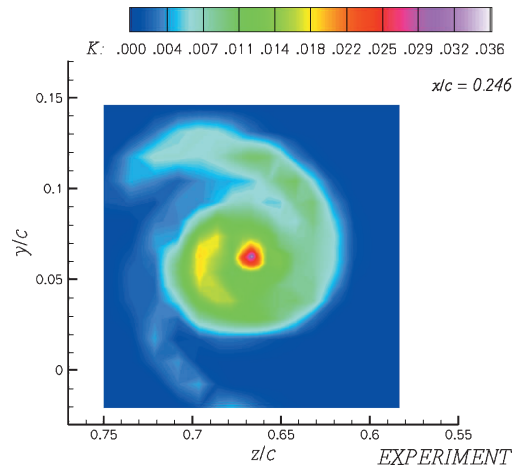
$$K = \frac{1}{2}\left(\langle u'u' + v'v' + w'w'\rangle / u_\infty^2\right) \qquad (17)$$

where u', v', and w' are the streamwise, transverse, and spanwise components of the fluctuating velocity, respectively; u_∞ is the freestream velocity and $\langle\ \rangle$ denotes time averaging. We first look at a crossflow plane upstream of the trailing edge, at $x/c = -0.114$. The experimental and LES turbulent kinetic energy contours are shown in Figs. 18 and 19, respectively. As can be seen from Figs. 18 and 19, the peak turbulent kinetic energy is found in the shear layer that departs from the surface and gets wrapped into the vortex. The location
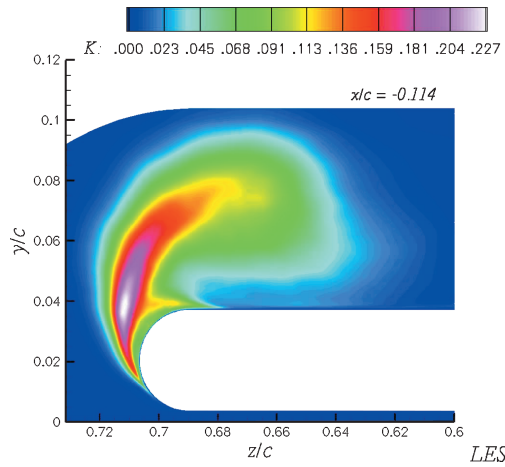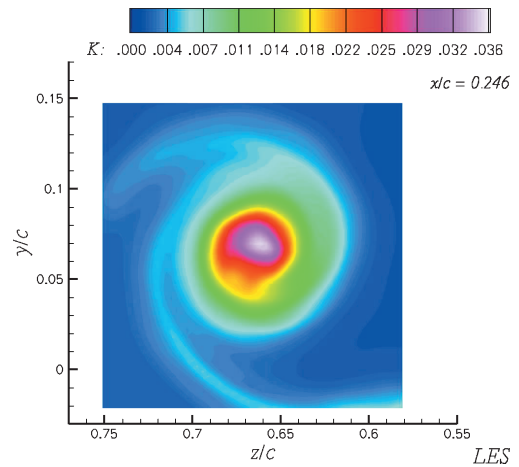
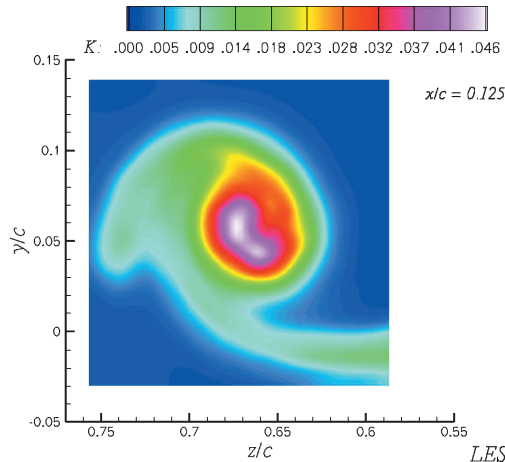Fig. 19   LES turbulent kinetic energy contours on crossflow plane at $x/c = -0.114$.

Fig. 20   Experimental turbulent kinetic energy contours on crossflow plane at $x/c = 0.125$.
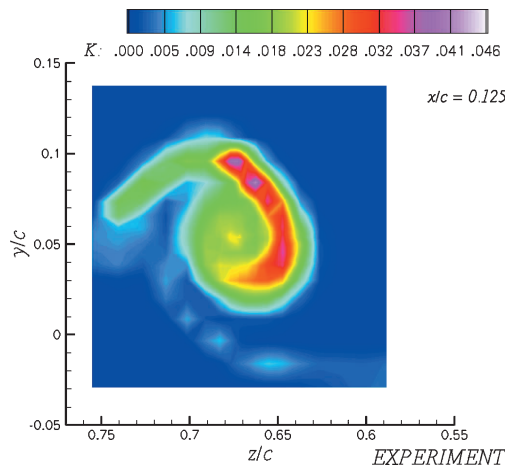
Fig. 21   LES turbulent kinetic energy contours on crossflow plane at $x/c = 0.125$.

Fig. 22   Experimental turbulent kinetic energy contours on crossflow plane at $x/c = 0.246$.

Fig. 23   LES turbulent kinetic energy contours on crossflow plane at $x/c = 0.246$.

of the peak turbulent kinetic energy is closer to the tip surface in the LES. Interestingly, the peak turbulent kinetic energy in the LES on this crossflow plane is almost four times that in the experiment. The differences observed here are not surprising because the earlier comparison of the crossflow streamlines on the same crossflow plane revealed significant differences between the LES and the experimental vortices during the initial roll up and formation. Next, we examine the turbulent kinetic contours on the $x/c = 0.125$ plane. The comparison at this location is shown in Figs. 20 and 21. This

time the peak turbulent kinetic energy in the experiment is found near the location of the maximum tangential velocity, which is approximately the edge of the viscous core, whereas in the LES, the peak turbulent kinetic energy is located inside the viscous core. Finally, the comparison at $x/c = 0.246$, shown in Figs. 22 and 23, reveals that the peak turbulent kinetic energy location in the experiment has shifted to a location inside the viscous core. The LES contours at this location also depict the peak location that is inside the viscous core. The LES and experimental peak turbulent kinetic energy levels in the planes downstream of the trailing edge are comparable to each other. Figure 24 shows the peak turbulent kinetic energy distribution along the streamwise direction. During the initial roll up and formation of the vortex upstream of the trailing edge, both the experimental and LES peak turbulent kinetic energy is found inside the detached shear layers getting wrapped into the vortex. However, in these planes upstream of the trailing edge, the LES clearly exhibits much higher turbulent kinetic energy. In the wake planes downstream of the trailing edge, we see that the LES peak turbulent kinetic energy inside the vortex matches the experimental values fairly well. The decay of the peak turbulent kinetic energy with increasing streamwise distance in the wake is due to the relaminarizing effect brought on by the nearly solid-body rotation of the viscous vortex core.[1] The viscous core is the innermost region of the vortex where viscosity causes the core to behave like a rotating solid body. This, in turn, results in a stabilizing effect that reduces the turbulence levels.

To answer the question as to why the LES predicts much higher turbulent kinetic energy in the detached shear layers upstream of the trailing edge, we need to examine the production term in the
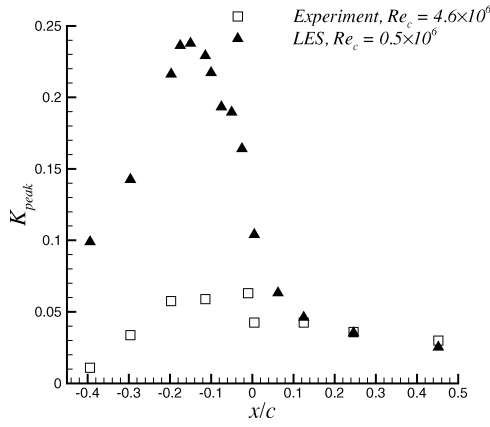
Fig. 24 Peak turbulent kinetic energy along streamwise direction; trailing edge of wing tip is at $x/c = 0$.

time-averaged turbulent kinetic energy transport equation

$$\frac{DK}{Dt} = \mathcal{P} - \mathcal{D} + \mathcal{T} \qquad (18)$$

where $\mathcal{P}$, $\mathcal{D}$, and $\mathcal{T}$ are the production, dissipation, and turbulent transport terms, respectively. The production term is given as

$$\mathcal{P} = -\left[\langle u'u' \rangle \frac{\partial \bar{u}}{\partial x} + \langle u'v' \rangle \left(\frac{\partial \bar{u}}{\partial y} + \frac{\partial \bar{v}}{\partial x} \right) + \langle v'v' \rangle \frac{\partial \bar{v}}{\partial y} + \langle v'w' \rangle \right.$$

$$\left. \times \left(\frac{\partial \bar{v}}{\partial z} + \frac{\partial \bar{w}}{\partial y} \right) + \langle w'w' \rangle \frac{\partial \bar{w}}{\partial z} + \langle u'w' \rangle \left(\frac{\partial \bar{u}}{\partial z} + \frac{\partial \bar{w}}{\partial x} \right) \right] \quad (19)$$

The production term represents the turbulent kinetic energy generation due to the interaction of the Reynolds stresses with the mean velocity gradients. The individual terms in the production equation can be either positive or negative. An analysis of the individual terms in this equation in conjunction with the simulation data yields the following observations:

1) The peak turbulent kinetic energy production takes place in the detached shear layers over the tip surface.

2) When the shear layer detaches from the tip surface over the upper half of the rounded tip, the most dominant term in Eq. (19) is $-\langle w'w' \rangle (\partial \bar{w}/\partial z)$.

3) When the shear layer detaches from the tip surface over the lower half of the rounded tip, the most dominant term in Eq. (19) is $-\langle v'v' \rangle (\partial \bar{v}/\partial y)$.

The first and the second observations are also supported by the experimental data. The third observation is not valid for the experiment because the shear layers in the experiment seem to detach over the upper half of the tip surface at all surface locations.

In the LES, during the initial formation of the tip vortex, the shear layers detach over the upper half of the tip surface. This is also true for the experiment. However, closer to the trailing edge, the shear layers in the LES detach over the lower half of the tip surface, whereas the experimental shear layers still appear to detach over the upper half of the tip surface. This discrepancy might again be a direct consequence of the Reynolds number difference because the higher-Reynolds-number shear layers are expected to stay attached to the surface a while longer before undergoing separation.

Figures 25 and 26 show the $-\langle w'w' \rangle (\partial \bar{w}/\partial z)$ production term contours on the crossflow plane at $x/c = -0.296$. This term is the most dominant term in the turbulent kinetic energy production on the $x/c = -0.296$ plane because the shear layers in both the LES and experiment detach over the upper half of the tip surface at this location. The peak value of this quantity is almost an order of magnitude larger in the LES, implying that the total turbulent kinetic energy production in the LES is significantly greater than the experiment. Also note here that because the experimental data were measured on a relatively coarse grid, the experimental $-\langle w'w' \rangle (\partial \bar{w}/\partial z)$ production term contours should be looked on with some caution due
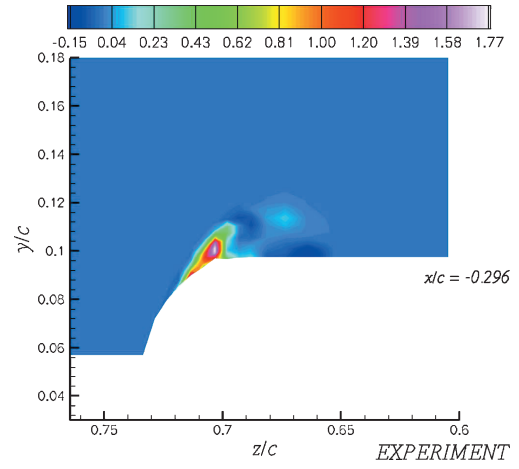

Fig. 25 Nondimensional $-\langle w'w' \rangle (\partial \bar{w}/\partial z)$ production term contours in experiment on crossflow plane at $x/c = -0.296$.
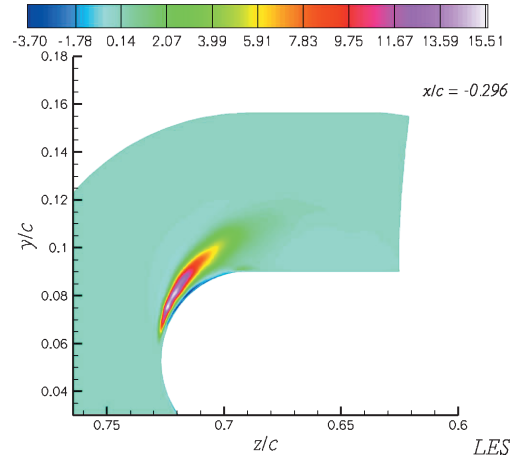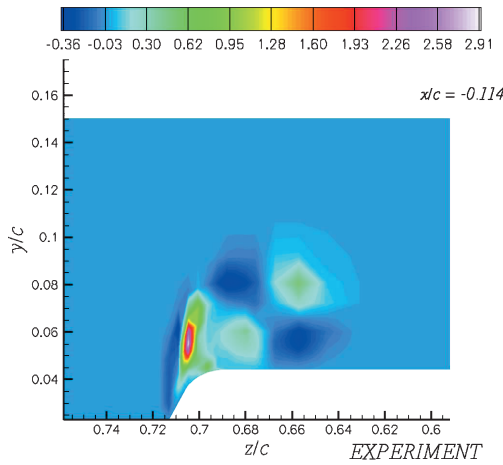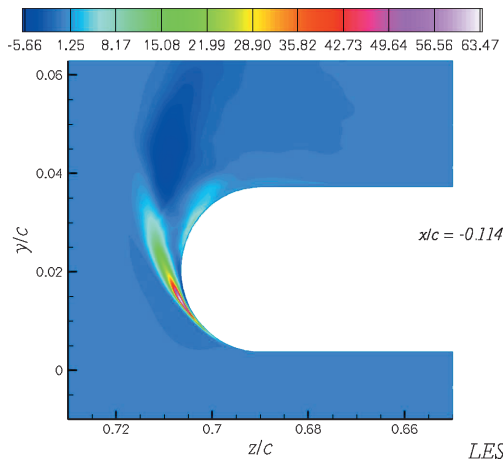

Fig. 26 Nondimensional $-\langle w'w' \rangle (\partial \bar{w}/\partial z)$ production term contours in LES on crossflow plane at $x/c = -0.296$.

to the possibility of a significant amount of error in the experimental mean velocity gradients. The peak turbulent kinetic energy production in the LES on this plane is about 96% of the peak value of the $-\langle w'w' \rangle (\partial \bar{w}/\partial z)$ term. Further analysis of the LES and experimental data shows that the magnitude of $(\partial \bar{w}/\partial z)$ at the peak production location in the LES is about 2.3 times larger than the value at the peak production location in the experiment, whereas the value of $\langle w'w' \rangle$ at the peak production location in the LES is about 3.8 times larger than that in the experiment. Examination of the unsteady flow data on several crossflow planes reveals that the shear layer separation points over the tip surface in the LES are not fixed. Hence, the higher value of $\langle w'w' \rangle$ is believed to be due to the oscillation of the shear layer separation point in the LES.

On the crossflow plane at $x/c = -0.114$, we see that the shear layer in the experiment still detaches over the upper half of the tip surface, and the most dominant term in the turbulent kinetic energy generation is again found to be $-\langle w'w' \rangle (\partial \bar{w}/\partial z)$. Figure 27 shows the contours of this quantity on the $x/c = -0.114$ plane. On the other hand, the LES shear layer detaches over the lower half of the tip surface on this crossflow plane, hence, the most dominant term in the turbulent kinetic energy generation becomes $-\langle v'v' \rangle (\partial \bar{v}/\partial y)$. Figure 28 shows the contours of this term on the $x/c = -0.114$ plane. As can be seen from Fig. 28, the peak value of this quantity is much larger than the peak value of the $-\langle w'w' \rangle (\partial \bar{w}/\partial z)$ term in the experiment on the same plane. Once again, this implies that the overall turbulent kinetic energy production in the LES on the given crossflow plane is much higher. The peak turbulent kinetic energy production in the LES on this plane is about 62% of the peak value of the $-\langle v'v' \rangle (\partial \bar{v}/\partial y)$ term. The magnitude of $(\partial \bar{v}/\partial y)$

Fig. 27 Nondimensional $-\langle w'w'\rangle(\partial\bar{w}/\partial z)$ **production term contours in experiment on crossflow plane at** $x/c = -0.114$.

Fig. 28 Nondimensional $-\langle v'v'\rangle(\partial\bar{v}/\partial y)$ **production term contours in LES on crossflow plane at** $x/c = -0.114$.

at the peak production location in the LES is about 5.5 times larger than the magnitude of $(\partial\bar{w}/\partial z)$ at the peak production location in the experiment, whereas the value of $\langle v'v'\rangle$ at the peak production location in the LES is about 3.9 times larger than the value of $\langle w'w'\rangle$ at the peak production location in the experiment.

In conclusion, the increased levels of turbulent kinetic energy generation in the LES are due to the larger values of $\langle w'w'\rangle$ or $\langle v'v'\rangle$, which result from the oscillation of the shear layer separation points, and the higher magnitude of $(\partial\bar{w}/\partial z)$ or $(\partial\bar{v}/\partial y)$ in the vicinity of the separated shear layers.

IV. Conclusions

A robust multiblock LES code utilizing state-of-the-art numerical methods has been developed. Results for the tip vortex around a nonrotating generic wing geometry with a rounded tip have been presented to demonstrate the capability of the code. The comparisons with the experiment suggest a strong Reynolds number influence on the initial vortex roll up as well as on the tip vortex mean flow and turbulence properties. The difference in the initial state of the LES and experimental boundary layers might also have contributed to some of the observed discrepancies. Nevertheless, good qualitative agreement between the LES and the experiment has been obtained in some of the comparisons.

To our best knowledge, the calculation presented herein is the first simulation of a tip vortex using an LES solver that employs high-order compact finite difference and filtering schemes in combination with an overset grid topology. Using the same code, we plan to compute the tip vortex noise for rotating realistic wind-turbine

blade tips. The near-field LES data will be coupled with the Ffowcs Williams–Hawkings method or a linearized Euler solver to compute the far-field noise. The simulations will be useful for studying the impact of the blade tip design on far-field noise and examining tip vortex noise generation mechanisms. Results from these simulations will be reported in the future.

Acknowledgments

References

[1]Chow, J., Zilliac, G., and Bradshaw, P., "Turbulence Measurements in the Near Field of a Wingtip Vortex," NASA TM 110418, Feb. 1997.

[2]Chow, J. S., "Turbulence Measurements in the Near-Field of a Wingtip Vortex," Ph.D. Dissertation, Dept. of Mechanical Engineering, Stanford Univ., Stanford, CA, Aug. 1994.

[3]Radeztsky, R. H., Singer, B. A., and Khorrami, M. R., "Detailed Measurements of a Flap Side-Edge Flow Field," AIAA Paper 98-0700, 1998.

[4]Dacles-Mariani, J., Zilliac, G. G., Chow, J. S., and Bradshaw, P., "Numerical/Experimental Study of a Wingtip Vortex in the Near Field," *AIAA Journal*, Vol. 33, No. 9, 1995, pp. 1561–1568.

[5]Dacles-Mariani, J., Kwak, D., and Zilliac, G., "On Numerical Errors and Turbulence Modeling in Tip Vortex Flow Prediction," *International Journal for Numerical Methods in Fluids*, Vol. 30, No. 1, 1999, pp. 65–82.

[6]Kim, S.-E., and Rhee, S. H., "Prediction of Tip-Vortex Flow past a Finite Wing," AIAA Paper 2005-0058, Jan. 2005.

[7]Takallu, M. A., and Laflin, K. R., "Reynolds-Averaged Navier–Stokes Simulations of Two Partial-Span Flap Wing Experiments," AIAA Paper 98-0701, 1998.

[8]Khorrami, M. R., Singer, B. A., and Radeztsky, R. H., "Reynolds Averaged Navier–Stokes Computations of a Flap Side-Edge Flow Field," AIAA Paper 98-0768, 1998.

[9]Fleig, O., Iida, M., and Arakawa, C., "Wind Turbine Blade Tip Flow and Noise Prediction by Large-Eddy Simulation," *Journal of Solar Energy Engineering*, Vol. 126, No. 4, 2004, pp. 1017–1024.

[10]Fleig, O., Iida, M., and Arakawa, C., "Wind Turbine Flow and Noise Prediction by Large Eddy Simulation," AIAA Paper 2005-1188, Jan. 2005.

[11]Cai, J., Deng, S., Xie, P., and Liu, C., "High-Order LES for Wing Tip Vortex in the Near Field," AIAA Paper 2005-1125, Jan. 2005.

[12]Ghias, R., Mittal, R., Dong, H., and Lund, T., "Study of Tip-Vortex Formation Using Large-Eddy Simulation," AIAA Paper 2005-1280, Jan. 2005.

[13]Imamura, T., Enomoto, S., Kato, H., Yokokawa, Y., and Yamamoto, K., "Numerical Simulation of NACA0012 Wingtip Flow Leading to Noise Generation," AIAA Paper 2005-2864, 2005.

[14]Mittal, R., and Moin, P., "Suitability of Upwind-Biased Finite Difference Schemes for Large-Eddy Simulation of Turbulent Flows," *AIAA Journal*, Vol. 35, No. 8, 1997, pp. 1415–1417.

[15]Visbal, M. R., and Gaitonde, D. V., "Very High-Order Spatially Implicit Schemes for Computational Acoustics on Curvilinear Meshes," *Journal of Computational Acoustics*, Vol. 9, No. 4, 2001, pp. 1259–1286.

[16]Ashcroft, G., and Zhang, X., "Optimized Prefactored Compact Schemes," *Journal of Computational Physics*, Vol. 190, No. 2, 2003, pp. 459–457.

[17]Uzun, A., "3-D Large Eddy Simulation for Jet Aeroacoustics," Ph.D. Dissertation, School of Aeronautics and Astronautics, Purdue Univ., West Lafayette, IN, Dec. 2003.

[18]Uzun, A., Blaisdell, G. A., and Lyrintzis, A. S., "Application of Compact Schemes to Large Eddy Simulation of Turbulent Jets," *Journal of Scientific Computing*, Vol. 21, No. 3, 2004, pp. 283–319.

[19]Uzun, A., Lyrintzis, A. S., and Blaisdell, G. A., "Coupling of Integral Acoustics Methods with LES for Jet Noise Prediction," *International Journal of Aeroacoustics*, Vol. 3, No. 4, 2004, pp. 297–346.

[20]Gaitonde, D. V., and Visbal, M. R., "Padé-Type Higher-Order Boundary Filters for the Navier–Stokes Equations," *AIAA Journal*, Vol. 38, No. 11, 2000, pp. 2103–2112.

[21]Lele, S. K., "Compact Finite Difference Schemes with Spectral-Like Resolution," *Journal of Computational Physics*, Vol. 103, No. 1, 1992, pp. 16–42.

[22]Beam, R. M., and Warming, R. F., "An Implicit Factored Scheme for the Compressible Navier–Stokes Equations," *AIAA Journal*, Vol. 16, No. 4, 1978, pp. 393–402.

[23]Ekaterinaris, J. A., "Implicit, High-Resolution, Compact Schemes for Gas Dynamics and Aeroacoustics," *Journal of Computational Physics*, Vol. 156, No. 2, 1999, pp. 272–299.

[24]Pulliam, T. H., "Artificial Dissipation Models for the Euler Equations," *AIAA Journal*, Vol. 24, No. 12, 1986, pp. 1931–1940.

[25]Tam, C. K. W., and Dong, Z., "Radiation and Outflow Boundary Conditions for Direct Computation of Acoustic and Flow Disturbances in a Nonuniform Mean Flow," *Journal of Computational Acoustics*, Vol. 4, No. 2, 1996, pp. 175–201.

[26]Bogey, C., and Bailly, C., "Three-Dimensional Non-Reflective Boundary Conditions for Acoustic Simulations: Far Field Formulation and Validation Test Cases," *Acta Acustica*, Vol. 88, No. 4, 2002, pp. 463–471.

[27]Kim, J. W., and Lee, D. J., "Generalized Characteristic Boundary Conditions for Computational Aeroacoustics," *AIAA Journal*, Vol. 38, No. 11, 2000, pp. 2040–2049.

[28]Kim, J. W., and Lee, D. J., "Generalized Characteristic Boundary Conditions for Computational Aeroacoustics, Part 2," *AIAA Journal*, Vol. 42, No. 1, 2004, pp. 47–55.

[29]Visbal, M. R., and Rizzetta, D. P., "Large-Eddy Simulation on Curvilinear Grids Using Compact Differencing and Filtering Schemes," *Journal of Fluids Engineering*, Vol. 124, No. 4, 2002, pp. 836–847.

[30]Visbal, M. R., Morgan, P. E., and Rizzetta, D. P., "An Implicit LES Approach Based on High-Order Compact Differencing and Filtering Schemes (Invited)," AIAA Paper 2003-4098, June 2003.

[31]Bogey, C., and Bailly, C., "Decrease of the Effective Reynolds Number with Eddy–Viscosity Subgrid-Scale Modeling," *AIAA Journal*, Vol. 43, No. 2, 2005, pp. 437–439.

[32]Benek, J. A., Steger, J. L., Dougherty, F. C., and Buning, P. G., "Chimera: A Grid-Embedding Technique," Arnold Engineering Development Center, Rept. AEDC-TR-85-64, Arnold Air Force Station, TN, April 1986.

[33]Henshaw, W., "Ogen: An Overlapping Grid Generator for Overture," Lawrence Livermore National Lab., Livermore, CA, URL: http://www.llnl.gov/casc/Overture [cited 24 June 2005].

[34]Sherer, S. E., and Scott, J. N., "High-Order Compact Finite-Difference Methods on General Overset Grids," *Journal of Computational Physics*, Vol. 210, No. 2, 2005, pp. 459–496.

[35]Sherer, S. E., "Investigation of High-Order and Optimized Interpolation Methods with Implementation in a High-Order Overset Grid Fluid Dynamics Solver," Ph.D. Dissertation, Dept. of Aeronautical and Astronautical Engineering, Ohio State Univ., Columbus, OH, Dec. 2002.

[36]Brentner, K. S., and Farassat, F., "Analytical Comparison of the Acoustic Analogy and Kirchhoff Formulation for Moving Surfaces," *AIAA Journal*, Vol. 36, No. 8, 1998, pp. 1379–1386.

[37]Chow, J. S., Zilliac, G. G., and Bradshaw, P., "Mean and Turbulence Measurements in the Near Field of a Wingtip Vortex," *AIAA Journal*, Vol. 35, No. 10, 1997, pp. 1561–1567.

[38]National Computational Science Alliance, Univ. of Illinois, Urbana, IL, URL: http://www.ncsa.uiuc.edu/UserInfo/Resources/Hardware/XeonCluster [cited 22 Feb. 2006].

[39]Tennekes, H., and Lumley, J. L., *A First Course in Turbulence*, MIT Press, Cambridge, MA, 1972, Chap. 5.

[40]Choi, H., and Moin, P., "Effects of the Computational Time Step on Numerical Solutions of Turbulent Flow," *Journal of Computational Physics*, Vol. 113, No. 1, 1994, pp. 1–4.

[41]McAlister, K. W., and Takahashi, R. T., "NACA 0015 Wing Pressure and Trailing Vortex Measurements," NASA TP 3151, Nov. 1991.

[42]Batchelor, G. K., "Axial Flow in Trailing Line Vortices," *Journal of Fluid Mechanics*, Vol. 20, No. 4, 1964, pp. 645–658.

D. Gaitonde
Associate Editor